Wave scattering by multiple rows of circular ice floes

L. G. BENNETTS† AND V. A. SQUIRE

Department of Mathematics and Statistics, University of Otago, PO Box 56,
Dunedin 9054, New Zealand

A three-dimensional model of ocean-wave scattering in the marginal ice zone is constructed using linear theory under time-harmonic conditions. Individual floes are represented by circular elastic plates and are permitted to have a physically realistic draught. These floes are arranged into a finite number of parallel rows, and each row possesses an infinite number of identical floes that are evenly spaced. The floe properties may differ between rows, and the spacing between the rows is arbitrary.

The vertical dependence of the solution is expanded in a finite number of modes, and through the use of a variational principle, a finite set of two-dimensional equations is generated from which the full-linear solution may be retrieved to any desired accuracy. By dictating the periodicity in each row to be identical, the scattering properties of the individual rows are combined using transfer matrices that take account of interactions between both propagating and evanescent waves.

Numerical results are presented that investigate the differences between using the three-dimensional model and using a two-dimensional model in which the rows are replaced with strips of ice. Furthermore, Bragg resonance is identified when the rows are identical and equi-spaced, and its reduction when the inhomogeneities, that are accommodated by the model, are introduced is shown.

---

1. Introduction

The marginal ice zone (MIZ) is defined as the area of sea ice that is significantly affected by open ocean processes. In practice this normally delineates an energetic region that extends several tens of kilometres from the ice edge into the pack ice, but it can sometimes reach to much greater distances when local ocean-wave activity is severe. The morphology of the MIZ is quite unlike that of the central Arctic Basin, where the sea-ice lamella is more continuous and is permeated by meandering imperfections such as pressure ridges and refrozen leads. In contrast, the MIZ is composed of many separate ice floes of different sizes and shapes that can move independently of their neighbours. In regard to floe size distribution, it is well documented that this mélange is created to a good degree by ocean waves travelling into the ice cover (see, for example, Squire *et al.* 1995; Squire 2007), while other natural processes act to redistribute the ice or hasten its demise through melting. Waves cause the floes to flex rhythmically with their passing, and when the bending is too great, the floes fracture. The ice floes tend to be smallest near the ice edge, where they are rapidly broken up by powerful incoming waves, sometimes being

---

† Email address for correspondence: lbennetts@maths.otago.ac.nz

pummelled to a slurry, and to increase in stages with distance from the edge until the destructive nature of the waves has been reduced sufficiently by scattering and other processes of attenuation so that the floes can reach much larger sizes and potentially fuse into sheet ice. While there are many MIZs, e.g. in the Greenland Sea, Barents Sea and Bering Sea in the sub-Arctic, the most sizable example occurs in the outer loci of the seasonal sea ice of the Southern Ocean surrounding the Antarctic continent, primarily because wave fetches to the north are so substantial. Of concern, as the effects of global climate change become established, is an alarming forewarning that MIZ conditions will become more prevalent (Rothrock, Yu & Maykut 1999; Cavalieri, Parkinson & Vinnikov 2003; Serreze, Holland & Stroeve 2007). This is because warmer temperatures and a higher frequency of storms with seas of greater intensity stimulate positive feedback due to associated ice albedo changes brought about by the presence of more open water and the concomitant enlarged injurious payload of penetrating ocean waves.

It is difficult to argue against the need for physical models that represent MIZ/ocean-wave interactions as accurately as possible, and which are capable of being tested against the few observations that are available (e.g. Wadhams *et al.* 1986, 1987). On entering the MIZ, ocean waves are scattered by each ice floe they encounter, but other processes, such as inelastic bending of the ice, hydrodynamical turbulence and wave-induced collisions, also act to a varying degree to remove energy from the wavetrain. Because in the MIZ the concentration and floe size distribution are heterogeneous, so too is the relative influence of each mechanism. Overall, wave energy appears to reduce exponentially with distance travelled, with the coefficient of attenuation being frequency dependent and discouraging the transmission of short waves. Directional isotropy is reached very quickly (Wadhams *et al.* 1986), although experiments have only been carried out in the immediate vicinity of the ice edge and at modest incursions and not in the ice interior in which some collation of the wave trains could potentially occur.

Formulating and solving the three-dimensional scattering problem that defines the evolution of waves in the MIZ is challenging, so most published studies have been two-dimensional (e.g. Kohout *et al.* 2007; Kohout & Meylan 2008) or have used Graf's interaction theory (e.g. Peter & Meylan 2004, 2007). There is some three-dimensional work (e.g. Chou 1998; Dixon & Squire 2001; Meylan & Masson 2006), but each analysis has deficiencies that limit its value as a predictive tool expressing how a three-dimensional wave field is altered by passage through the MIZ. This paper is a further step towards minimizing the shortcomings inherent in these earlier models.

For a situation as complicated as the one described above a number of assumptions are required in order to construct a mathematical representation. From the outset linearized theory will be applied and time-harmonic conditions imposed. Furthermore, in keeping with the current wisdom, the floes are modelled using thin-plate theory, which is justified, as sea ice in the MIZ has horizontal dimensions that far exceed its thickness. In response to fluid motion, a floe therefore bends and flexes and, in doing so, transports energy in the form of flexural-gravity waves, which appear as oscillations at the fluid–ice interface. Sea ice, in the guise of a thin, elastic plate, is described in terms of a mass and a flexural rigidity as well as in terms of its spatial dimensions, and its influence on the mathematical problem comes in the form of a high-order surface condition.

A situation, typical in the MIZ, is envisaged in which an ocean wave penetrates into a region occupied by an array of floes. Each floe in the array is set in motion by this wave but is also acted upon by the waves that are diffracted by all of the other

floes in the array. There is therefore a simultaneous dependency of the floes on one another that is intrinsic in the scattering problem. As the incident wave travels deeper into the ice pack it becomes increasingly attenuated due to interactions with the floes, and in this way the MIZ can protect the landfast sea-ice abutting the coast and, potentially, any ice shelves that they border from being destroyed, e.g. the Wilkins on the Antarctic Peninsula. (Note that the latter is the stimulus for the Cooperative Institute for Research in Environmental Sciences' Innovative Research Program 'Is Absence of Sea Ice a Causal Factor in Recent Antarctic Ice Shelf Break-Ups?')

The idealized array that is considered in this work is made up of a finite number of rows, where each row contains an infinite number of identical and equally spaced circular floes. However, the properties of the floes may differ between the rows. Individual rows, with various permutations, have been considered previously by a number of authors. For the current work the solution method of Bennetts & Squire (in press) is particularly helpful, and a modified version of it will be utilized. This relies on the implementation of an approximation method, capable of producing the full-linear solution to any given accuracy, which is generated through the combination of a variational principle and an expansion of the vertical motion of the problem. Calculation of the resulting approximation here uses an identity that vastly reduces the numerical calculations needed in comparison to the original method of Bennetts & Squire and also allows the irregular frequencies, which could otherwise cause numerical instability, to be captured.

Each row in the array supports a finite number of propagating waves that travel at known angles and an infinite number of evanescent waves that decay away from the rows, and, for a given row, the relationships between these waves are defined via a scattering matrix that gives the reflected amplitudes in terms of those of the incoming waves or, alternatively, by a transfer matrix that relates amplitudes on either side of the row. By restricting the spacing within the rows so that waves supported by the array, between each pair of adjacent rows, match the single-row problem, the representations derived for the individual rows will be superposed using transfer matrices to produce the solution for the entire array in an iterative manner. This method, which has been used previously by Porter & Porter (2001) for free-surface flows over periodic bedforms, is numerically efficient and also will allow for some analytical insight to be gained.

Having set out the governing equations of linear motion and the approximation method in the following section, in §3 we outline our solution method. This is subdivided into the reappraised solution of the single-row problem and the interaction theory for multiple rows using transfer matrices. The special case of a homogeneous array, comprised of identical and equally spaced rows, is treated in §3.5, as further simplifications arise that benefit analysis of the numerical results in §4. Initially though, the numerical results given compare the three-dimensional model that will be devised in this paper to an analogous two-dimensional model and highlight their different reflection properties. The full interaction theory is then compared to a wide-spacing approximation (WSA) that assumes that only propagating waves exist between rows, and it is found that very little information is lost by making such an approximation. During §4 a homogeneous array will be seen to support Bragg resonance, and it is this feature with which the WSA facilitates analysis. The final set of results investigate how each of the inhomogeneities that the model admits diminish these unphysical occurrences.

While the model we present in this paper is not a perfect replica of scattering in the MIZ, essentially because of the periodicities that are intrinsic to the formulation,

we do allow each row of floes to be different from the next and we do incorporate draught properly. These are major complications that bring us closer to having a model that can faithfully represent the MIZ when acted upon by ocean waves and eventually be incorporated into global climate models.

2. Preliminaries and multi-mode expansion

Consider a fluid domain of infinite horizontal extent, which is bounded below by a flat and finite bed. The geometry is described in terms of the Cartesian coordinates $x \equiv (x, y) \in \mathbb{R}^2$ in the horizontal plane and z in the vertical plane, which points upwards. In the absence of ice cover the fluid domain occupies the interval $z \in (-h, 0)$, where $z = -h$ is the position of the seabed. By fixing this surface to be flat our model ignores the varying seabed as an additional source of scattering, but this is justified, as the situations that we are interested in will occur in deep water, and thus undulations on the ocean floor will be negligible in comparison to the presence of ice.

On the otherwise free fluid surface floats an array of ice floes composed of a finite number, say M, of straight rows, each containing an infinite number of floes, which, without loss of generality, we assume to be orientated so that they lie parallel to the y-axis. The rows are then defined as finite intervals of x that are non-overlapping. We count the rows in ascending order with respect to the x-axis and denote $a_{m-} < x < a_{m+}$ as the interval occupied by row m.

For solution purposes, we apply a periodicity condition that fixes the distance between the floes and requires the floes in a particular row to be identical, although the floes may differ between the rows. In the present work we will assume that the floes are circular and of constant thickness and finite draught, although the interaction theory that we outline in this work is valid for more general floe geometries. In row m the radius of the floes is denoted a_m, with their thickness, which is considered known, given by $D = D_m$ and their equilibrium submergence then being $d = d_m = (\rho_i/\rho_w)D_m = 0.9D_m$ in order to satisfy the Archimedean principle, where $\rho_i = 922.5 \, \text{kg m}^{-3}$ is the density of the ice and $\rho_w = 1025 \, \text{kg m}^{-3}$ is the density of the fluid.

Let the distance between the 'centre' of each adjacent floe in the same row be $2y_0$, where y_0 is a chosen constant. The problem is therefore identical for any given channel in which the domain is restricted in the y-direction to the finite length $2y_0$. Of course it would also be straightforward to consider rows in which the spacing is an integer multiple of $2y_0$, but we will be content to restrict ourselves to the case of equal spacing in this work.

Finally, we set the centre of one of the floes in the mth row to coincide with the point $x = x_m \equiv (x_m, y_m)$, where, clearly, it is possible to restrict y_m to the interval $-y_0 < y_m < y_0$. We therefore note that $a_{m\pm} = x_m \pm a_m$. The geometrical configuration that has just been described is depicted in figures 1 and 2.

Under the regular assumptions of linear motions and time-harmonic conditions, we seek the properties of the fluid from the reduced velocity potential $P = P(x, y, z)$, where $(\partial_x, \partial_y, \partial_z)\text{Re}\{(g/i\omega)(Pe^{-i\omega t})\}$ defines the velocity field. Here ω is a prescribed angular frequency and $g \approx 9.81 \, \text{m s}^{-2}$ is the acceleration due to gravity. For all points x in the horizontal plane, P must satisfy Laplace's equation

$$\nabla^2 P + \partial_z^2 P = 0 \quad (x \in \mathbb{R}^2, -h < z < -d), \tag{2.1}$$

in the fluid domain, where $\nabla \equiv (\partial_x, \partial_y)$, and for convenience, we have extended the definition of the function d to $d = 0$ when ice cover is absent. On the impermeable bed the no-flow condition $\partial_z P = 0$ $(z = -h)$ is imposed. For those regions in which
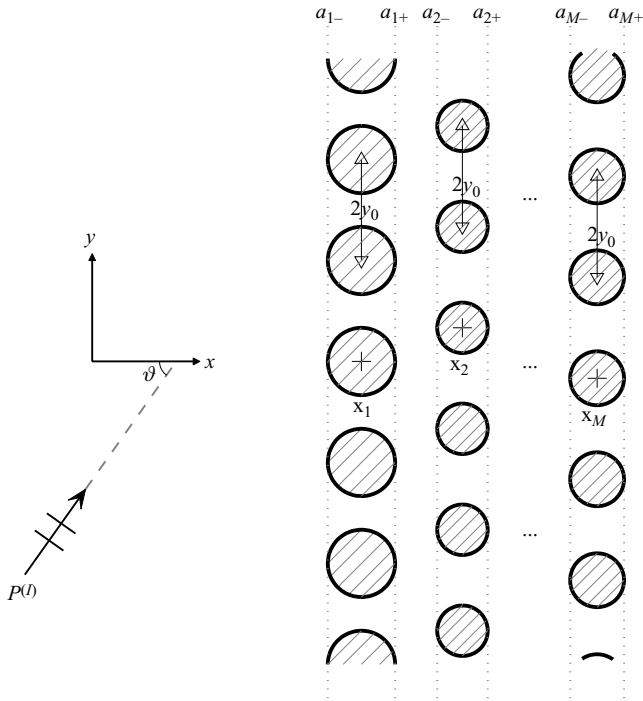
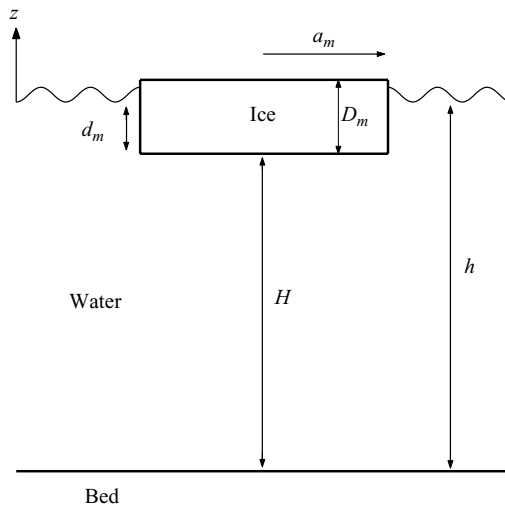FIGURE 1. Schematic showing the geometry in the horizontal plane.

FIGURE 2. Schematic showing a cross-section that includes a single floe from row m.

the fluid surface is not occupied by ice, the free-surface condition $\partial_z P = \sigma P$ $(z = 0)$ holds, where $\sigma = \omega^2/g$ is a frequency parameter.

A plane wave $P^{(I)}$ propagates from the far field $x \to -\infty$ towards the array at the oblique angle ϑ with respect to the x-axis, so that it may be written

$$P^{(I)} = P^{(I)}(\boldsymbol{x}, z) = e^{i(v_{0,0}(x-x_1)+u_0 y)} \cosh\{k_0(z+h)\},$$

where $u_0 = k_0 \sin \vartheta$, $v_{0,0} = k_0 \cos \vartheta$ and the quantity k_0 is the propagating wavenumber that will be defined shortly. In response to this forcing, the array scatters a finite number of propagating waves, and the far field takes the form

$$P(\boldsymbol{x}, z) \sim \left\{ e^{i(v_{0,0}(x-x_1)+u_0 y)} + \sum_{q \in Q} R_q e^{i(-v_{0,q}(x-x_1)+u_q y)} \right\} \cosh\{k_0(z+h)\} \qquad (2.2a)$$

as $x \to -\infty$ and

$$P(\boldsymbol{x}, z) \sim \left\{ \sum_{q \in Q} T_q e^{i(v_{0,q}(x-x_M)+u_q y)} \right\} \cosh\{k_0(z+h)\} \qquad (2.2b)$$

as $x \to \infty$. Here the quantities $u_q = u_0 + pq$, where $p = \pi/y_0$ and $v_{0,q} = \sqrt{\{k_0^2 - u_q^2\}}$. We use Q to denote the subset of integers for which the $v_{0,q}$ are real. In the above expressions R_q and T_q define the amplitudes of the reflected and transmitted waves respectively and must be obtained as part of the solution process.

When forced by the incident wave, the ice cover itself experiences small-scale oscillations. We define the resulting position of the underside of the ice cover to be

$$z = -d + \mathrm{Re}\{W e^{-i\omega t}\} \quad (\boldsymbol{x} \in \mathscr{D}),$$

where the displacement function $W = W(\boldsymbol{x})$ must be found as part of the solution process and $\mathscr{D}$ defines the subset of the horizontal plane in which the fluid is ice covered. The fluid motion is coupled with the ice displacement through the equations

$$(1 - \sigma d)W + F\nabla^4 W - P = 0 \quad (\boldsymbol{x} \in \mathscr{D}, \, z = -d) \qquad (2.3a)$$

and

$$\nabla d \cdot \nabla P + \partial_z P = 0 \quad (\boldsymbol{x} \in \mathscr{D}, \, z = -d). \qquad (2.3b)$$

In the former of the above equations the quantity $F = YD^3/12(1 - \nu^2)\rho_w g$ denotes the scaled flexural rigidity of the ice. Further parameters have been introduced in this definition; they are Poisson's ratio $\nu = 0.3$ and Young's modulus for ice $Y = 5 \times 10^9$ Pa.

Due to the complexity that is presented by the geometry in this problem, we choose to apply the multi-mode approximation (MMA) derived by Bennetts *et al.* (2007). In order to form this approximation the unknown functions are defined through a variational principle that is equivalent to Laplace's equation (2.1), the free-surface and bed conditions and the plate equations (2.3*a,b*). This is combined with an expansion of the vertical dependence of the velocity potential, P, in a finite number of vertical modes, which then allows the variational principle to average vertically and, in doing so, generate a new set of governing equations from which we obtain the MMA. Although it has no vertical dependence, the displacement function is indirectly approximated in the MMA through its relation to the potential, and we write $w \approx W$.

By taking a sufficient number of vertical modes to represent the vertical motion, the full-linear solution may be found to any chosen degree of accuracy. However, it has been shown previously that only a relatively small number of modes are needed to produce accurate results (see Bennetts *et al.* 2009*b*, for example) so that the solution will be obtained at a low numerical cost.

To invoke the MMA we therefore write

$$P(\boldsymbol{x}, z) \approx \begin{cases} \phi(\boldsymbol{x}, z) = \displaystyle\sum_{n=0}^{N} \phi_n(\boldsymbol{x})\zeta_n(z) \quad (\boldsymbol{x} \in \mathbb{R}^2/\mathscr{D}), \\[3mm] \psi(\boldsymbol{x}, z) = \displaystyle\sum_{n=0}^{N} \psi_n(\boldsymbol{x})\chi_n(z) \quad (\boldsymbol{x} \in \mathscr{D}). \end{cases} \tag{2.4}$$

The above approximation has caused a partitioning of the solution into the separate free-surface and ice-covered fluid domains, through the respective expansions in the vertical modes $\zeta_n(z) = \cosh\{k_n(z+h)\}$ and $\chi_n(z) = \cosh\{\kappa_n(z+h)\}$. Here, the quantities k_n are the roots k of the free-surface dispersion relation

$$k \tanh(kh) = \sigma,$$

with k_0 real and positive and k_n $(n = 1, \ldots, N)$ purely imaginary and ordered such that $0 < -\mathrm{i}k_n < -\mathrm{i}k_{n+1}$. The quantities κ_n are the roots κ of the ice-covered dispersion relation

$$(1 - \sigma d + F\kappa^4)\kappa \tanh(\kappa H) = \sigma,$$

where $H = h - d$ denotes the fluid depth beneath the ice. As with the roots of the free-surface dispersion relation, we set κ_0 to be the unique real, positive root and κ_n $(n = 1, \ldots, N)$ to be the roots that lie on the positive imaginary axis and order them in increasing magnitude. The complex roots of the ice-covered dispersion relation can be ignored when creating approximation (2.4) (see Bennetts *et al.* 2007 for details). Changing the thickness of the ice causes the values of d, F and H to change, and thus the roots κ_n $(n = 0, \ldots, N)$ may vary between the rows.

As the primary mode in the free-surface fluid domain, ζ_0, is that which supports propagating waves, we are able to represent the incident wave exactly in our approximation, and this allows the radiation conditions to be defined as

$$\phi_0(\boldsymbol{x}) \sim \begin{cases} \mathrm{e}^{\mathrm{i}(v_{0,0}(x-x_1)+u_0 y)} + \displaystyle\sum_{q\in Q} R_q \mathrm{e}^{\mathrm{i}(-v_{0,q}(x-x_1)+u_q y)} & (x \to -\infty), \\[3mm] \displaystyle\sum_{q\in Q} T_q \mathrm{e}^{\mathrm{i}(v_{0,q}(x-x_M)+u_q y)} & (x \to \infty), \end{cases} \tag{2.5}$$

and $\phi_n \sim 0$ as $x \to \pm\infty$ $(n = 1, \ldots, N)$. Therefore, the only inaccuracies inherent in the far-field form of the MMA come through the approximate values that will be found for the reflection and transmission coefficients, R_q and T_q.

In the free-surface region, it remains to solve the Helmholtz equations

$$\nabla^2 \boldsymbol{\Phi} + \boldsymbol{K}_-^2 \boldsymbol{\Phi} = 0 \quad (\boldsymbol{x} \in \mathbb{R}^2/\mathscr{D}),$$

where the vector of solutions $\boldsymbol{\Phi} = \boldsymbol{\Phi}(\boldsymbol{x}) = (\phi_0(\boldsymbol{x}), \ldots, \phi_N(\boldsymbol{x}))^T$ and the matrix $\boldsymbol{K}_- = \mathrm{diag}\{k_0, \ldots, k_N\}$. For the domain $\mathscr{D}$, in which the fluid is ice covered, we now have the system of second-order equations

$$\boldsymbol{C}_0 \nabla^2 \boldsymbol{\Psi} + \boldsymbol{C}_1 \boldsymbol{\Psi} + \sigma \boldsymbol{C} \boldsymbol{f} w = 0 \quad (\boldsymbol{x} \in \mathscr{D}),$$

which is coupled with a fourth-order equation

$$(1 - \sigma d)w + F\nabla^4 w - \boldsymbol{f}^T \boldsymbol{C} \boldsymbol{\Psi} = 0 \quad (\boldsymbol{x} \in \mathscr{D}).$$

Here, the vector of unknowns is $\boldsymbol{\Psi} = \boldsymbol{\Psi}(\boldsymbol{x}) = (\psi_0(\boldsymbol{x}), \ldots, \psi_N(\boldsymbol{x}))^T$, and we define the $(N+1)$-length vector $\boldsymbol{f} = (1, \ldots, 1)^T$ and matrix $\boldsymbol{C} = \mathrm{diag}\{\cosh(\kappa_0 H), \ldots, \cosh(\kappa_N H)\}$.

The matrices of coefficients $\mathbf{C}_j$ ($j = 0, 1$) contain averaged values of the vertical dependence, and their entries are given by

$$\{\mathbf{C}_0\}_{j+1,i+1} = \int_{-h}^{-d} \chi_j \chi_i \, dz, \quad \{\mathbf{C}_1\}_{j+1,i+1} = \int_{-h}^{-d} \chi_j \frac{d^2 \chi_i}{dz^2} \, dz - \left[\chi_j \frac{d\chi_i}{dz} \right]_{z=-h}^{-d}$$

for $i, j = 0, \ldots, N$.

On the boundary of $\mathscr{D}$, say Γ, which divides the region of ice-covered fluid from the region of free-surface fluid, the continuity of fluid pressure and velocity beneath the edges of the floes cannot be exactly retained in the MMA. Instead jump conditions, which are provided by the variational principle, must be applied. These are

$$\mathbf{C}_+^T \mathbf{\Psi} = \mathbf{C}_-^T \mathbf{\Phi}, \quad \mathbf{C}_+^{-1} \mathbf{C}_0 \partial_n \mathbf{\Psi} = \mathbf{C}_-^{-1} \mathbf{C}_2 \partial_n \mathbf{\Phi} \quad (\mathbf{x} \in \Gamma), \tag{2.7}$$

where

$$\{\mathbf{C}_+\}_{j+1,i+1} = \int_{-h}^{-d} \chi_j \cosh\{\kappa_i(z + h)\} \, dz, \quad \{\mathbf{C}_-\}_{j+1,i+1} = \int_{-h}^{-d} \zeta_j \cosh\{\kappa_i(z + h)\} \, dz$$

and

$$\{\mathbf{C}_2\}_{j+1,i+1} = \int_{-h}^{0} \zeta_j \zeta_i \, dz,$$

for $i, j = 0, \ldots, N$.

The approximate displacement w must satisfy dynamical conditions at the ice edges to ensure that the bending moment and shearing stress vanish at these points, and these are expressed as $\mathscr{B}w = 0$ and $\mathscr{S}w = 0$ respectively, where

$$\mathscr{B}w \equiv \nabla^2 w - (1 - \nu) \left(\partial_s^2 w + \frac{d\Theta}{ds}(\partial_n w) \right) \tag{2.8a}$$

and

$$\mathscr{S}w \equiv \partial_n \nabla^2 w + (1 - \nu)\partial_s \left((\partial_s \partial_n w) - \frac{d\Theta}{ds}(\partial_s w) \right). \tag{2.8b}$$

In the above equations $\partial_s = \mathbf{s} \cdot \nabla$ and $\partial_n = \mathbf{n} \cdot \nabla$, with $\mathbf{s}$ a unit vector tangential to the edge and $\mathbf{n}$ a normal vector that points away from the particular floe and has direction cosines $(\cos \Theta, \sin \Theta)$ ($\Theta = \Theta(s)$) with respect to the horizontal Cartesian frame.

It is now necessary to calculate the vectors of unknowns $\mathbf{\Phi}$ and $\mathbf{\Psi}$ and the function w from (2.5)–(2.8) in order to define our approximation of the velocity potential (2.4) and of the displacement function. A method for achieving this will be outlined in the following section.

3. Formulation

3.1. *A single row*

Let us begin with the case of a single row ($M = 1$). The interaction of multiple rows will then be calculated through a composition of these single-row solutions. For a single row there is no need to use subscripts to identify quantities as belonging to a particular row, and we therefore abandon them until extra rows are added.

Without loss of generality, at this stage we may suppose that one of the floes is centred on the origin $\mathbf{x} = 0$. Using the inherent periodicities of the solution, namely

that

$$\boldsymbol{\Phi}(x, y + y_0) = e^{2iu_0 y_0}\boldsymbol{\Phi}(x, y - y_0), \quad \partial_y\boldsymbol{\Phi}(x, y + y_0) = e^{2iu_0 y_0}\partial_y\boldsymbol{\Phi}(x, y - y_0),$$

we recast the problem in the channel $\Omega_0 = \{\boldsymbol{x} : x \in \mathbb{R}, -y_0 < y < y_0\}$ that contains only one floe, which is located in the disk $\mathcal{D}_0 = \{\boldsymbol{x} : |\boldsymbol{x}| < a\}$ and with suitable phase-change conditions applied on the finite boundaries $y = \pm y_0$. It is then a simple matter to extend to any point outside of this channel by using the periodicity of the solution.

The unknown functions will be expressed in terms of their values on the circular boundary $\Gamma_0 = \{\boldsymbol{x} : |\boldsymbol{x}| = a\}$ at which the free-surface fluid meets the ice-covered fluid within the channel. On this interface the solutions are calculated in the form of the following Fourier expansions:

$$[\boldsymbol{\Phi}]_{\Gamma_0} \approx \sum_{m=-m_0}^{m_0} \boldsymbol{\Phi}_m e^{im\theta}, \quad [\boldsymbol{\Psi}]_{\Gamma_0} \approx \sum_{m=-m_0}^{m_0} \boldsymbol{\Psi}_m e^{im\theta},$$

where $\theta \in [0, 2\pi)$ is the regular azimuthal coordinate. The expansions are truncated at the finite value m_0, which is chosen to gain sufficient accuracy.

Within the circular domain of ice-covered fluid it is natural to use polar coordinates, and seeking a separation solution gives

$$\boldsymbol{\Psi}(\boldsymbol{x}) \approx \sum_{m=-m_0}^{m_0} \left\{ \widehat{\boldsymbol{J}}_m(r) + \sum_{i=1,2} \boldsymbol{v}_i \boldsymbol{c}_{m,i}^T J_m(\mu_i r) \right\} \boldsymbol{A}_m e^{im\theta} \quad (\boldsymbol{x} \in \mathcal{D}_0), \tag{3.1}$$

where r is the radial coordinate $r = \sqrt{(x^2 + y^2)}$ and the vectors $\boldsymbol{A}_m$ are of length $N + 1$ and contain, as yet, unknown constants. In expression (3.1) the function J_m denotes the Bessel function of the first kind of order m, which is also contained in the the diagonal matrix $\widehat{\boldsymbol{J}}_m(r) = \text{diag}\{J_m(\kappa_0 r), \dots, J_m(\kappa_N r)\}$. We calculate the quantities μ_i $(i = 1, 2)$ as the roots μ of the fourth-order equation

$$(F\mu^4 + 1 - \sigma d) + F\boldsymbol{f}^T \boldsymbol{C}\boldsymbol{C}_0^{-1}(\boldsymbol{K}_+^2 + \mu^2 I)\boldsymbol{K}_+\boldsymbol{S}_+\boldsymbol{f} = 0,$$

where $\boldsymbol{K}_+ = \text{diag}\{\kappa_0, \dots, \kappa_N\}$ and $\boldsymbol{S}_+ = \text{diag}\{\sinh(\kappa_0 H), \dots, \sinh(\kappa_N H)\}$, which lie in the upper-half complex plane, and the corresponding vectors of length $N + 1$, $\boldsymbol{v}_i$, from

$$\boldsymbol{C}_0\boldsymbol{v}_i + F(\boldsymbol{K}_+^2 + \mu_i^2 I)\boldsymbol{K}_+\boldsymbol{S}_+\boldsymbol{f} = 0 \quad (i = 1, 2).$$

The role of the motion associated to μ_i and $\boldsymbol{v}_i$ is in approximating the oscillatory–evanescent waves that are supported by ice-covered fluid (see Bennetts *et al.* 2007). There are a further set of vectors of length $N + 1$ involved in the definition of $\boldsymbol{\Psi}$, namely $\boldsymbol{c}_{m,i}$ $(i = 1, 2)$, and these are chosen so that the corresponding representation of the displacement function

$$w(\boldsymbol{x}) \approx \sum_{m=-m_0}^{m_0} \left\{ \sigma^{-1}\boldsymbol{f}^T \boldsymbol{K}_+\boldsymbol{S}_+\widehat{\boldsymbol{J}}_m(r) + \sum_{i=1,2} \boldsymbol{c}_{m,i}^T J_m(\mu_i r) \right\} \boldsymbol{A}_m e^{im\theta},$$

satisfies the dynamic conditions (2.8*a,b*) on Γ_0.

In the free-surface domain the vector of unknowns, $\boldsymbol{\Phi}$, is written in the form of an integral representation,

$$\boldsymbol{\Phi}(\boldsymbol{x}) \approx \boldsymbol{\Phi}^{(I)}(\boldsymbol{x}) - a \sum_{m=-m_0}^{m_0} \int_0^{2\pi} \boldsymbol{G} e^{im\tau} \, \mathrm{d}\tau \{\boldsymbol{J}_m'(a)(\boldsymbol{J}_m(a))^{-1}\boldsymbol{\Phi}_m - \boldsymbol{\Phi}_m'\}, \tag{3.2}$$

for $x \in \Omega_0/\mathscr{D}_0$, where $\boldsymbol{\Phi}^{(I)}$ is the forcing vector (left unspecified for the present), $\boldsymbol{\Phi}'_m$ are the coefficients of the Fourier expansion of $[\partial_r \boldsymbol{\Phi}]_{\Gamma_0}$ and $\mathbf{G} = \mathbf{G}(x|\tau)$ is a matrix of Green's functions. The above representation incorporates a further diagonal matrix of Bessel functions, namely $\boldsymbol{J}_m(r) = \mathrm{diag}\{J_m(k_0 r), \ldots, J_m(k_N r)\}$, and a prime on these matrices indicates differentiation with respect to the radial coordinate.

It is now possible to calculate the unknown quantities $\boldsymbol{\Phi}_m$ and $\boldsymbol{\Psi}_m$ ($m = -m_0, \ldots, m_0$) by evaluating expressions (3.1) and (3.2) on Γ_0 and using the jump conditions (2.7). Once these have been calculated, it is possible to retrieve the solution at all points.

By using an integral representation for the solution in the free-surface region, as in (3.2), Bennetts & Squire (in press) constructed a solution method for a single row of identical ice floes that vary axisymmetrically in thickness, and the details of the matrix of Green's functions, $\mathbf{G}$, and the calculation of the integrals in which it appears may be found therein. However, unlike this previous work, in which it was also necessary to calculate integrals involving the radial derivative of the matrix of Green's functions, the derivation of (3.2) makes use of the identity

$$\boldsymbol{J}_m(a) \int_0^{2\pi} [\partial_r \mathbf{G}]_{r=a} \mathrm{e}^{im\tau}\, \mathrm{d}\tau - \boldsymbol{J}'_m(a) \int_0^{2\pi} [\mathbf{G}]_{r=a} \mathrm{e}^{im\tau}\, \mathrm{d}\tau = \frac{1}{2a} \boldsymbol{J}_m(a) \mathrm{e}^{im\theta}$$

to eliminate such integrals, and this constitutes a substantial numerical saving. A similar identity can be shown to hold for the analogous matrix of Green's functions for an unbounded domain, defined as

$$\mathbf{G}_0(x|X) = \frac{1}{4i} \mathrm{diag}\{H_0(k_0|x - X|), \ldots, H_0(k_N|x - X|)\},$$

where H_0 is the Hankel function of the first-kind order zero, and the above result for the matrix of quasi-periodic Green's functions, $\mathbf{G}$, then follows by expressing it as a sum of images of $\mathbf{G}_0$ (see Linton 1998 for example), so that

$$\mathbf{G}(x|\tau) = \sum_{m=-\infty}^{\infty} \mathbf{G}_0(x|X_m) \mathrm{e}^{-2imu_0 y_0},$$

where $X_m = (a\cos\tau, 2my_0 + a\sin\tau)$.

Our new expression also exposes the irregular frequencies of the integral representation, evaluated on the boundary Γ_0, as occurring when $J_m(k_0 a) = 0$ for some m. At these points a solution could be obtained by instead using the radial derivative of (3.2), although we will be content to simply skip them in the current work.

We also note that there exist resonant frequencies when the periodicity is such that $v_{0,q} = 0$ for some q. Such a value indicates that there is a wave that travels parallel to the array. A means of solving for these isolated frequencies is described in Linton & Thompson (2007), and although we do not pursue such an idea here, their method could be adapted to our solution procedure.

3.2. Scattering and transfer matrices

Interactions between adjacent rows consist of both propagating and evanescent waves, and in order to implement the solution method for a single row, outlined in the previous section, we must allow for a forcing vector $\boldsymbol{\Phi}^{(I)}$ that accommodates these

waves. Therefore, we write

$$\boldsymbol{\Phi}^{(I)}(\boldsymbol{x}) = \sum_{j=-J}^{J} \left\{ \mathrm{e}^{\mathrm{i}\boldsymbol{V}_j x} \boldsymbol{A}_j^{(-)} + \mathrm{e}^{-\mathrm{i}\boldsymbol{V}_j x} \boldsymbol{A}_j^{(+)} \right\} \mathrm{e}^{\mathrm{i}u_j y},$$

where the vectors $\boldsymbol{A}_j^{(\pm)}$ denote the incident amplitudes and J is a finite number that will be chosen large enough to accurately represent the interactions between adjacent rows. The diagonal matrix $\mathrm{e}^{\pm \mathrm{i}\boldsymbol{V}_j x} = \mathrm{diag}\{\mathrm{e}^{\pm \mathrm{i}v_{0,j}x}, \dots, \mathrm{e}^{\pm \mathrm{i}v_{N,j}x}\}$, in which the values $v_{n,j} = \sqrt{\{k_n^2 - u_j^2\}}$ $(n = 0, \dots, N; j = -J, \dots, J)$ extend the definition of $v_{0,q}$ $(q \in Q)$ given earlier. For $q \in Q$ the values $v_{0,q}$ are real and the corresponding functions $\mathrm{e}^{\pm \mathrm{i}v_{0,q}x}$ represent propagating waves that travel at different angles. All other values of $v_{n,j}$ are purely imaginary and define evanescent waves.

The solution $\boldsymbol{\Phi}$ is then similarly decomposed as

$$\boldsymbol{\Phi}(\boldsymbol{x}) = \sum_{j=-J}^{J} \left\{ \left[\boldsymbol{\Phi}_{0,j}^{(-)}(\boldsymbol{x}) \dots \boldsymbol{\Phi}_{N,j}^{(-)}(\boldsymbol{x}) \right] \boldsymbol{A}_j^{(-)} + \left[\boldsymbol{\Phi}_{0,j}^{(+)}(\boldsymbol{x}) \dots \boldsymbol{\Phi}_{N,j}^{(+)}(\boldsymbol{x}) \right] \boldsymbol{A}_j^{(+)} \right\}, \tag{3.3}$$

where each of the $(N + 1)$-length vectors $\boldsymbol{\Phi}_{n,j}^{(\pm)}$ is a solution of the single-row problem for the incident wave $\boldsymbol{\Phi}_{n,j}^{(I\pm)} = \mathrm{e}^{\pm \mathrm{i}\boldsymbol{V}_j x} \boldsymbol{I}_n \mathrm{e}^{\mathrm{i}u_j y}$, in which $\boldsymbol{I}_n$ represents the $(n+1)$th column of the $(N + 1)$-dimensional identity matrix.

For $|x| > a$ the solutions $\boldsymbol{\Phi}_{n,p}^{(\pm)}$ may be written in the form

$$\boldsymbol{\Phi}_{n,p}^{(-)}(\boldsymbol{x}) = \begin{cases} \mathrm{e}^{\mathrm{i}\boldsymbol{V}_p x} \boldsymbol{I}_n \mathrm{e}^{\mathrm{i}u_p y} + \displaystyle\sum_{j=-J}^{J} \mathrm{e}^{-\mathrm{i}\boldsymbol{V}_j x} \boldsymbol{R}_{n,p,j}^{(-)} \mathrm{e}^{\mathrm{i}u_j y} & (x \leqslant -a), \\[4mm] \displaystyle\sum_{j=-J}^{J} \mathrm{e}^{\mathrm{i}\boldsymbol{V}_j x} \boldsymbol{T}_{n,p,j}^{(-)} \mathrm{e}^{\mathrm{i}u_j y} & (x \geqslant a) \end{cases} \tag{3.4a}$$

and

$$\boldsymbol{\Phi}_{n,p}^{(+)}(\boldsymbol{x}) = \begin{cases} \displaystyle\sum_{j=-J}^{J} \mathrm{e}^{-\mathrm{i}\boldsymbol{V}_j x} \boldsymbol{T}_{n,p,j}^{(+)} \mathrm{e}^{\mathrm{i}u_j y} & (x \leqslant -a), \\[4mm] \mathrm{e}^{-\mathrm{i}\boldsymbol{V}_p x} \boldsymbol{I}_n \mathrm{e}^{\mathrm{i}u_p y} + \displaystyle\sum_{j=-J}^{J} \mathrm{e}^{\mathrm{i}\boldsymbol{V}_j x} \boldsymbol{R}_{n,p,j}^{(+)} \mathrm{e}^{\mathrm{i}u_j y} & (x \geqslant a). \end{cases} \tag{3.4b}$$

The values of the $(N + 1)$-length vectors of reflection coefficients $\boldsymbol{R}_{n,p,j}^{(\pm)}$ and transmission coefficients $\boldsymbol{T}_{n,p,j}^{(\pm)}$ $(n = 0, \dots, N; p, j = -J, \dots, J)$ are calculated through integral (3.2) as described in Bennetts & Squire. Similarly, the full solution may be expanded as

$$\boldsymbol{\Phi}(\boldsymbol{x}) = \begin{cases} \displaystyle\sum_{j=-J}^{J} \left\{ \mathrm{e}^{\mathrm{i}\boldsymbol{V}_j x} \boldsymbol{A}_j^{(-)} + \mathrm{e}^{-\mathrm{i}\boldsymbol{V}_j x} \boldsymbol{B}_j^{(-)} \right\} \mathrm{e}^{\mathrm{i}u_j y} & (x \leqslant -a), \\[4mm] \displaystyle\sum_{j=-J}^{J} \left\{ \mathrm{e}^{\mathrm{i}\boldsymbol{V}_j x} \boldsymbol{A}_j^{(+)} + \mathrm{e}^{-\mathrm{i}\boldsymbol{V}_j x} \boldsymbol{B}_j^{(+)} \right\} \mathrm{e}^{\mathrm{i}u_j y} & (x \geqslant a), \end{cases} \tag{3.5}$$

in which the $(N + 1)$-length vectors $\boldsymbol{B}_j^{(\pm)}$ $(j = -J, \dots, J)$ contain the scattered amplitudes.

By comparing (3.3) and (3.4*a,b*) to (3.5) it is easily seen that the relationship between the incident amplitudes and scattered amplitudes for a single row may be represented through a scattering matrix $\boldsymbol{S}$, which is defined by

$$\begin{pmatrix} \boldsymbol{B}^{(-)} \\ \boldsymbol{B}^{(+)} \end{pmatrix} = \boldsymbol{S} \begin{pmatrix} \boldsymbol{A}^{(-)} \\ \boldsymbol{A}^{(+)} \end{pmatrix}, \quad \boldsymbol{S} = \begin{pmatrix} \boldsymbol{R}^{(-)} & \boldsymbol{T}^{(-)} \\ \boldsymbol{T}^{(+)} & \boldsymbol{R}^{(+)} \end{pmatrix}. \tag{3.6}$$

Here, the $(2J+1)(N+1)$-length vectors

$$\boldsymbol{A}^{(\pm)} = \begin{pmatrix} \boldsymbol{A}_{-J}^{(\pm)} \\ \vdots \\ \boldsymbol{A}_{J}^{(\pm)} \end{pmatrix}, \quad \boldsymbol{B}^{(\pm)} = \begin{pmatrix} \boldsymbol{B}_{-J}^{(\pm)} \\ \vdots \\ \boldsymbol{B}_{J}^{(\pm)} \end{pmatrix}$$

amalgamate the incident and scattered amplitudes respectively, and the $(2J+1)(N+1)$-dimensional square matrices $\boldsymbol{R}^{(\pm)}$ and $\boldsymbol{T}^{(\pm)}$ contain the reflection and transmission coefficients, with

$$\boldsymbol{R}^{(\pm)} = \begin{pmatrix} \hat{\boldsymbol{R}}_{-J,-J}^{(\pm)} & \cdots & \hat{\boldsymbol{R}}_{-J,J}^{(\pm)} \\ \vdots & & \vdots \\ \hat{\boldsymbol{R}}_{J,-J}^{(\pm)} & \cdots & \hat{\boldsymbol{R}}_{J,J}^{(\pm)} \end{pmatrix}, \quad \hat{\boldsymbol{R}}_{p,q}^{(\pm)} = \begin{pmatrix} R_{0,p,q}^{(\pm)} & \cdots & R_{N,p,q}^{(\pm)} \end{pmatrix}$$

and

$$\boldsymbol{T}^{(\pm)} = \begin{pmatrix} \hat{\boldsymbol{T}}_{-J,-J}^{(\pm)} & \cdots & \hat{\boldsymbol{T}}_{-J,J}^{(\pm)} \\ \vdots & & \vdots \\ \hat{\boldsymbol{T}}_{J,-J}^{(\pm)} & \cdots & \hat{\boldsymbol{T}}_{J,J}^{(\pm)} \end{pmatrix}, \quad \hat{\boldsymbol{T}}_{p,q}^{(\pm)} = \begin{pmatrix} T_{0,p,q}^{(\pm)} & \cdots & T_{N,p,q}^{(\pm)} \end{pmatrix}.$$

Due to the symmetry of the circular floes we note that the simplifications $\boldsymbol{R}^{(-)} = \boldsymbol{R}^{(+)}$ and $\boldsymbol{T}^{(-)} = \boldsymbol{T}^{(+)}$ hold.

Equivalently, we may calculate a transfer matrix $\boldsymbol{P}$ that relates the amplitudes for $x \geqslant a$ to those for $x \leqslant -a$, with

$$\begin{pmatrix} \boldsymbol{A}^{(+)} \\ \boldsymbol{B}^{(+)} \end{pmatrix} = \boldsymbol{P} \begin{pmatrix} \boldsymbol{B}^{(-)} \\ \boldsymbol{A}^{(-)} \end{pmatrix}.$$

The transfer matrix may be obtained from the scattering matrix $\boldsymbol{S}$ and vice versa by using the second component of (3.6) and

$$\boldsymbol{P} = \begin{pmatrix} \boldsymbol{T}^{(-)} - \boldsymbol{R}^{(+)}\mathrm{inv}(\boldsymbol{T}^{(+)})\boldsymbol{R}^{(-)} & \boldsymbol{R}^{(+)}\mathrm{inv}(\boldsymbol{T}^{(+)}) \\ -\mathrm{inv}(\boldsymbol{T}^{(+)})\boldsymbol{R}^{(-)} & \mathrm{inv}(\boldsymbol{T}^{(+)}) \end{pmatrix}. \tag{3.7}$$

By extending the results on the scattering matrix for a single row that were given in Bennetts & Squire to include evanescent waves, it may be deduced that due to the symmetry of the circular floes, the eigenvalues of the transfer matrix $\boldsymbol{P}$ arise in reciprocal pairs and also in complex-conjugate pairs. This result will be of use at a later stage.

3.3. *Multiple rows*

Now consider the case in which there is more than one row in the array $(M > 1)$. For the mth row we may expand the solution as in (3.5) between the edges of the row

and the nearest edge of each of the corresponding adjacent rows and write

$$\Phi(x) = \begin{cases} \displaystyle\sum_{j=-J}^{J} \left\{ e^{i\mathbf{v}_j(x-x_m)} \mathbf{r}_j^{(m-)} + e^{-i\mathbf{v}_j(x-x_m)} \mathbf{l}_j^{(m-)} \right\} e^{iu_j y} & (a_{m-1+} \leqslant x \leqslant a_{m-}), \\[2ex] \displaystyle\sum_{j=-J}^{J} \left\{ e^{i\mathbf{v}_j(x-x_m)} \mathbf{r}_j^{(m+)} + e^{-i\mathbf{v}_j(x-x_m)} \mathbf{l}_j^{(m+)} \right\} e^{iu_j y} & (a_{m+} \leqslant x \leqslant a_{m+1-}). \end{cases} \tag{3.8}$$

For the first or last rows ($m = 1, M$) the relevant limit is removed, so that $a_{0+} \leqslant x \leqslant a_{1-}$ becomes simply $x \leqslant a_{1-}$ for example. The vectors $\mathbf{r}_j^{(m\pm)}$ and $\mathbf{l}_j^{(m\pm)}$ ($m = 1, \ldots, M$; $j = -J, \ldots, J$) denote the amplitudes of the rightward- and leftward-travelling waves to the left-hand side ($-$) and right-hand side ($+$) of row m (with respect to the x-axis). Currently these amplitudes are unknown.

It is straightforward to translate the mth row so that one of its constituent floes is centred at the origin by using the coordinates $\tilde{x} = x - x_m$, which allows the problem posed by this row alone to be solved (up to the as yet unknown incident amplitudes) using the method described in §3.1. For each row then, the scattering and transfer matrices, $\mathbf{S}_m = \mathbf{Y}_m \tilde{\mathbf{S}}_m \mathbf{Y}_m^{-1}$ and $\mathbf{P}_m = \mathbf{Y}_m \tilde{\mathbf{P}}_m \mathbf{Y}_m^{-1}$ respectively may be calculated, for which

$$\begin{pmatrix} \mathbf{l}^{(m-)} \\ \mathbf{r}^{(m+)} \end{pmatrix} = \mathbf{S}_m \begin{pmatrix} \mathbf{r}^{(m-)} \\ \mathbf{l}^{(m+)} \end{pmatrix}, \qquad \begin{pmatrix} \mathbf{r}^{(m+)} \\ \mathbf{l}^{(m+)} \end{pmatrix} = \mathbf{P}_m \begin{pmatrix} \mathbf{r}^{(m-)} \\ \mathbf{l}^{(m-)} \end{pmatrix}, \tag{3.9}$$

for $m = 1, \ldots, M$, where the amplitudes of (3.8) are amalgamated in the vectors $\mathbf{r}^{(m\pm)}$ and $\mathbf{l}^{(m\pm)}$, with

$$\mathbf{r}^{(m\pm)} = \begin{pmatrix} \mathbf{r}_{-J}^{(m\pm)} \\ \vdots \\ \mathbf{r}_J^{(m\pm)} \end{pmatrix}, \qquad \mathbf{l}^{(m\pm)} = \begin{pmatrix} \mathbf{l}_{-J}^{(m\pm)} \\ \vdots \\ \mathbf{l}_J^{(m\pm)} \end{pmatrix} \qquad (m = 1, \ldots, M).$$

The appearance of the $2(N+1)(2J+1)$-square matrix $\mathbf{Y}_m$ in the above is due to the shift of the array in the y-direction and is defined by

$$\mathbf{Y}_m = \text{diag}\{ e^{iu_{-J} y_m} \mathbf{f}^T, \ldots, e^{iu_J y_m} \mathbf{f}^T, e^{iu_{-J} y_m} \mathbf{f}^T, \ldots, e^{iu_J y_m} \mathbf{f}^T \}.$$

Equation (3.9) yields a set of relations that will be used to find the unknown amplitudes.

At present we do not have enough information, in (3.9) alone, to calculate the vectors $\mathbf{r}^{(m\pm)}$ and $\mathbf{l}^{(m\pm)}$ ($m = 1, \ldots, M$) that will fully define our solution. However, note that in (3.8) we have two expressions for each of the intervals between adjacent floes. Equating these gives the relations

$$\mathbf{r}^{(m+1-)} = e^{i\mathbf{v}l_m} \mathbf{r}^{(m+)}, \qquad \mathbf{l}^{(m+1-)} = e^{-i\mathbf{v}l_m} \mathbf{l}^{(m+)}, \tag{3.10}$$

for $m = 1, \ldots, M-1$, where the $(N+1)(2J+1)$-square matrix

$$e^{i\mathbf{v}l_m} = \text{diag}\{ e^{i\mathbf{v}_{-J} l_m}, \ldots, e^{i\mathbf{v}_J l_m} \}$$

and the scalar values $l_m = x_{m+1} - x_m$ denote the distances between rows. The amplitudes in expression (3.8) that do not belong to waves that exist between rows may be equated to either the incident amplitudes

$$\mathbf{r}^{(1-)} = \mathbf{I}_0, \qquad \mathbf{l}^{(M+)} = 0$$

or the amplitudes of the waves scattered away from the array, for which we write $l^{(1-)} = R$ for the reflected waves and $r^{(M+)} = T$ for the transmitted waves. Note that these vectors contain the amplitudes of the evanescent waves as well as those of the propagating ones. There are now a sufficient number of equations to match the unknown amplitudes.

3.4. *Solution through iteration*

Transfer matrices give us a convenient way to combine the interaction of the rows in an iterative manner, so that the solution for $m + 1$ rows can be deduced from that of m rows. This method reduces the numerical expense by both avoiding inversion of increasingly large matrices when rows are appended to the array and allowing previous solutions to be reused when studying the effects of additional rows.

Henceforth, let the transfer matrix that operates over the rows p to q $(p < q)$ be defined as $P_{p,q}$, that is

$$\begin{pmatrix} r^{(q+)} \\ l^{(q+)} \end{pmatrix} = P_{p,q} \begin{pmatrix} r^{(p-)} \\ l^{(p-)} \end{pmatrix},$$

and let the matrices

$$X_m = \begin{pmatrix} e^{i V l_m} & 0 \\ 0 & e^{-i V l_m} \end{pmatrix} \quad (m = 1, \ldots, M - 1),$$

define the phase changes (3.10) that occur between the rows. If an extra row is appended to the right-hand side of this array then the corresponding transfer matrix, $P_{p,q+1}$, may be deduced by operating the transfer matrix for the $(q + 1)$th row alone, P_{q+1}, and the phase change matrix between the qth and $(q + 1)$th rows, X_q, on $P_{p,q}$, so that

$$P_{p,q+1} = P_{q+1} X_q P_{p,q}. \tag{3.11}$$

For each of these transfer matrices there is an associated scattering matrix, and we denote the scattering matrix that operates over the rows p to q as $S_{p,q}$, for which

$$\begin{pmatrix} l^{(p-)} \\ r^{(q+)} \end{pmatrix} = S_{p,q} \begin{pmatrix} r^{(p-)} \\ l^{(q+)} \end{pmatrix}, \quad S_{p,q} = \begin{pmatrix} R_{p,q}^{(-)} & T_{p,q}^{(-)} \\ T_{p,q}^{(+)} & R_{p,q}^{(+)} \end{pmatrix}.$$

As previously stated, the scattering matrix may be obtained from the transfer matrix through (3.6) and (3.7), and using this approach with the form for $P_{p,q+1}$ given above, we find that the entries of the scattering matrix $S_{p,q+1}$ are

$$R_{p,q+1}^{(-)} = R_{p,q}^{(-)} + T_{p,q}^{(+)} e^{i V l_q} \left(I - R_{q+1}^{(-)} e^{i V l_q} R_{p,q}^{(+)} e^{i V l_q} \right)^{-1} R_{q+1}^{(-)} e^{i V l_q} T_{p,q}^{(-)}, \tag{3.12a}$$

$$T_{p,q+1}^{(-)} = T_{p,q}^{(+)} e^{i V l_q} \left(I - R_{q+1}^{(-)} e^{i V l_q} R_{p,q}^{(+)} e^{i V l_q} \right)^{-1} T_{q+1}^{(+)}, \tag{3.12b}$$

$$R_{p,q+1}^{(+)} = R_{q+1}^{(+)} + T_{q+1}^{(-)} e^{i V l_q} \left(I - R_{p,q}^{(+)} e^{i V l_q} R_{q+1}^{(-)} e^{i V l_q} \right)^{-1} R_{p,q}^{(+)} e^{i V l_q} T_{q+1}^{(+)} \tag{3.12c}$$

and

$$T_{p,q+1}^{(+)} = T_{q+1}^{(-)} e^{i V l_q} \left(I - R_{p,q}^{(+)} e^{i V l_q} R_{q+1}^{(-)} e^{i V l_q} \right)^{-1} T_{p,q}^{(-)}, \tag{3.12d}$$

where the matrices $R_j^{(\pm)}$ and $T_j^{(\pm)}$ contain the reflected and transmitted coefficients for the jth row. The above relationships mirror those derived for flows over two-dimensional ripple beds by Chamberlain & Porter (1995) and electromagnetic scattering by periodic arrays of cylinders by McPhedran *et al.* (1999).

The transfer and scattering matrices for the entire M rows, $P_{1,M}$ and $S_{1,M}$ respectively, may now be iteratively calculated using the above relations, moving

from left to right and beginning at row 1, noting that $\boldsymbol{P}_{1,1} \equiv \boldsymbol{P}_1$ and $\boldsymbol{S}_{1,1} \equiv \boldsymbol{S}_1$. At this point we are able to use $\boldsymbol{S}_{1,M}$ to calculate the scattered amplitudes $\boldsymbol{R}$ and $\boldsymbol{T}$, which defines the scattering characteristics of the full array.

Alternatively, we could calculate $\boldsymbol{P}_{1,M}$ and $\boldsymbol{S}_{1,M}$ by working from right to left and beginning at row M, for which $\boldsymbol{P}_{M,M} \equiv \boldsymbol{P}_M$ and $\boldsymbol{S}_{M,M} \equiv \boldsymbol{S}_M$, using relations similar to (3.12a–d) that are based on $\boldsymbol{P}_{p-1,q} = \boldsymbol{P}_{p,q}\boldsymbol{X}_{p-1}\boldsymbol{P}_{p-1}$. These alternative left-to-right and right-to-left methods may then be combined to produce the amplitudes within the array in terms of the incident amplitudes alone. Using the transfer matrix that operates from row 1 to row m with that which operates from row m to row M we find that

$$\boldsymbol{r}^{(m-)} = \left(I - \boldsymbol{R}_{1,m}^{(+)}\mathrm{e}^{\mathrm{i}\boldsymbol{V}l_m}\boldsymbol{R}_{m+1,M}^{(-)}\mathrm{e}^{\mathrm{i}\boldsymbol{V}l_m}\right)^{-1}\left\{\boldsymbol{T}_{1,m}^{(-)}\boldsymbol{r}^{(1-)} + \boldsymbol{R}_{1,m}^{(+)}\mathrm{e}^{\mathrm{i}\boldsymbol{V}l_m}\boldsymbol{T}_{m+1,M}^{(+)}\boldsymbol{l}^{(M+)}\right\}$$

and

$$\boldsymbol{l}^{(m+1+)} = \left(I - \boldsymbol{R}_{m+1,M}^{(-)}\mathrm{e}^{\mathrm{i}\boldsymbol{V}l_m}\boldsymbol{R}_{1,m}^{(+)}\mathrm{e}^{\mathrm{i}\boldsymbol{V}l_m}\right)^{-1}\left\{\boldsymbol{R}_{m+1,M}^{(-)}\mathrm{e}^{\mathrm{i}\boldsymbol{V}l_m}\boldsymbol{T}_{1,m}^{(-)}\boldsymbol{r}^{(1-)} + \boldsymbol{T}_{m+1,M}^{(+)}\boldsymbol{l}^{(M+)}\right\},$$

for $m = 1, \ldots, M-1$, with the corresponding amplitudes $\boldsymbol{r}^{(m+)}$ and $\boldsymbol{l}^{(m-)}$ then calculated through simple phase changes.

3.5. *The homogeneous problem*

If the rows that we are considering are aligned and contain identical floes, so that $\boldsymbol{P}_i = \boldsymbol{P}_j \equiv \boldsymbol{P}$ ($i, j = 1, \ldots, M$), and are equally spaced, so that $l_i = l_j \equiv l$ and $\boldsymbol{X}_i = \boldsymbol{X}_j \equiv \boldsymbol{X}$ ($i, j = 1, \ldots, M-1$), then we can simplify the expression for the transfer matrix $\boldsymbol{P}_{1,M}$. With these restrictions in place, (3.11) gives

$$\boldsymbol{P}_{1,M} = \boldsymbol{X}^{-1/2}\widehat{\boldsymbol{P}}^M\boldsymbol{X}^{-1/2}, \quad \widehat{\boldsymbol{P}} = \boldsymbol{X}^{1/2}\boldsymbol{P}\boldsymbol{X}^{1/2}.$$

By using the properties of the eigenvalues of the transfer matrix for a single row stated earlier, which are consequences of the symmetry of the geometry, we may adopt the diagonalization

$$\widehat{\boldsymbol{P}} = \boldsymbol{H}\begin{pmatrix} \Delta & 0 \\ 0 & \Delta^{-1} \end{pmatrix}\boldsymbol{H}^{-1},$$

in which the matrix $\boldsymbol{H}$ contains the eigenvectors of $\widehat{\boldsymbol{P}}$ and Δ its eigenvalues that lie either within the unit circle or on the upper half of the unit circle. Therefore, the above expression for the transfer matrix simplifies further still to

$$\boldsymbol{P}_{1,M} = \boldsymbol{X}^{-1/2}\boldsymbol{H}\begin{pmatrix} \Delta^M & 0 \\ 0 & \Delta^{-M} \end{pmatrix}\boldsymbol{H}^{-1}\boldsymbol{X}^{-1/2}.$$

The scattering matrix may then be calculated from $\boldsymbol{P}_{1,M}$ as

$$\boldsymbol{S}_{1,M} = -\widehat{\boldsymbol{X}}\begin{pmatrix} \boldsymbol{H}_1 & -\Delta^M\boldsymbol{H}_2 \\ \Delta^M\boldsymbol{H}_2 & -\boldsymbol{H}_1 \end{pmatrix}^{-1}\begin{pmatrix} \boldsymbol{H}_2 & -\Delta^M\boldsymbol{H}_1 \\ \Delta^M\boldsymbol{H}_1 & -\boldsymbol{H}_2 \end{pmatrix}\widehat{\boldsymbol{X}}, \tag{3.14}$$

where

$$\widehat{\boldsymbol{X}} = \begin{pmatrix} \mathrm{e}^{-\mathrm{i}\boldsymbol{V}l/2} & 0 \\ 0 & \mathrm{e}^{-\mathrm{i}\boldsymbol{V}l/2} \end{pmatrix}, \quad \boldsymbol{H}^{-1} = \begin{pmatrix} \boldsymbol{H}_1 & \boldsymbol{H}_2 \\ \boldsymbol{H}_2 & \boldsymbol{H}_1 \end{pmatrix}.$$

This strategy (devised by Porter & Porter 2001) is numerically stable, as it avoids use of the growing terms that are present in Δ^{-M}. The above forms for the transfer and scattering matrices will be of use in the following section to help analyse the resonances found during numerical simulations.

4. Numerical results

The results presented in this section are all non-dimensionalized with respect to the periodicity length scale $2y_0$. It is therefore only necessary to quote the non-dimensional incident wavenumber $\tilde{k}_0 = 2y_0 k_0$, floe radii $\tilde{a}_m = a_m/2y_0$, ice thicknesses $\tilde{D}_m = D_m/2y_0$, fluid depth $\tilde{h} = h/2y_0$ and row centres $\tilde{x}_m = x_m/2y_0$ ($m = 1, \dots, M$) in order to define a problem. Note also that the Young's modulus must be scaled as $Y/2y_0$. For clarity, the tilde notation that has just been introduced to define the non-dimensional parameters will be dropped. The non-dimensional fluid depth, which is of subordinate importance in our upcoming investigation, is set as $h = 0.4$.

During this section we will often refer to the full approximation. This indicates that we have used a sufficient number of evanescent waves in the interaction theory to ensure that our approximation has converged to the full-linear solution to a desired accuracy. The number of evanescent waves that must be considered will vary according to a number of parameters, in particular the wave frequency. Here, the maximum number of vertical modes that we consider is $N = 16$, and the maximum truncation on the waves supported by each vertical mode is $J = 2$. Of course, the dimension of the vertical space we implement also controls the accuracy of the solution for the individual rows.

Previous studies of the propagation of waves through the MIZ (see Kohout *et al.* 2007, for example) have been based on two-dimensional models, thus assuming no variation of the ice cover in one spatial dimension. The geometry is therefore composed of strips of ice, and it is of interest to observe how these models compare with the one considered in this work, in which the MIZ is idealized as an array of individual floes.

Using the solution method of Bennetts *et al.* (2007) for a single two-dimensional floe, it is possible to replace the periodic arrays of rows in the current problem with strips of ice. The interaction theory is then, in fact, merely a degenerate case of the multiple-row problem, as in the two-dimensional model, waves may propagate only in a single direction.

In figure 3 we compare results for identical and equi-spaced rows of floes to those of the analogous problem in which the intervals $a_{m-} < x < a_{m+}$ ($m = 1, \dots, M$) contain strips of ice. Six cases are displayed. In each there are six rows (or strips) and the ice is of non-dimensional thickness $D \equiv D_m = 0.02$ ($m = 1, \dots M$), with the rows (or strips) separated so that $l \equiv l_m = 0.2$ ($m = 1, \dots M - 1$). We investigate the non-dimensional values of radius $a \equiv a_m = 0.15$, 0.3 and 0.45 ($m = 1, \dots M$) and the incident angles $\vartheta = 0$ and $60°$.

The quantity E that is displayed in figure 3 is the normalized energy reflected in the direction of the primary reflected wave, defined by $E = (1/v_{0,0}) \sum_{q \in Q} v_{0,q} |R_q|^2$, and is plotted as a continuous function of the scaled (non-dimensional) wavenumber $K = k_0/\pi$. It is clear in all cases that the strips of ice generally reflect a larger proportion of the incident wave than the rows of floes. As would be expected, this feature is strongest for the smaller values of the non-dimensional radius, for which the floes are smaller and there is a wider spacing of the floes within the rows.

For the normally incident waves, the qualitative nature of the reflection produced by the rows is similar to that of the strips, with the respective maxima often closely matching in position and proportion. It can be noted however that for $K > 2$ when $a = 0.45$, while the strips attain total reflection, $E \approx 1$, there is still a fine structure present in the energy reflected by the rows, possibly due to the many length scales that exist in this model. On the contrary, for the obliquely incident wave, we see vastly different results given by the rows and the strips. This is largely due to the rapid
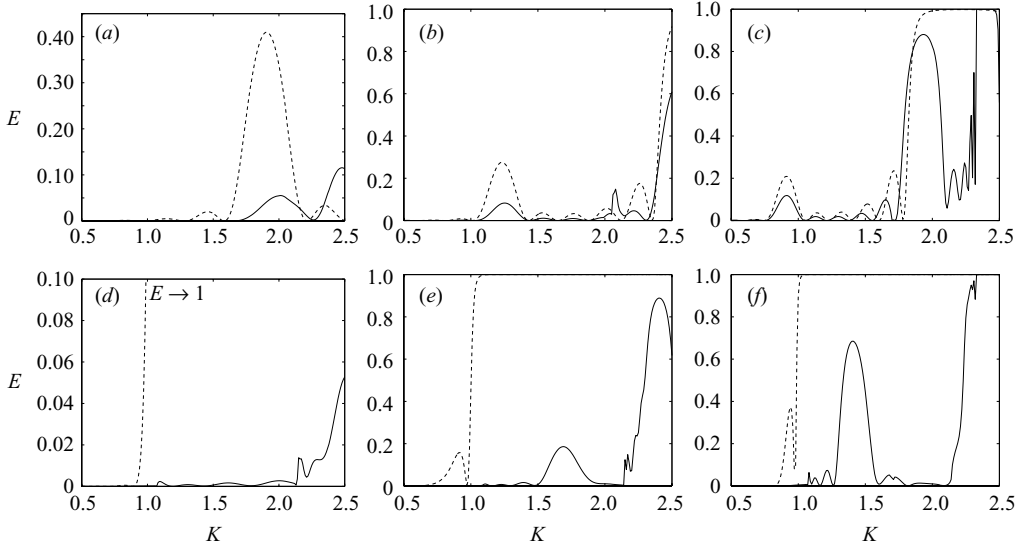
FIGURE 3. Comparison of the energy E reflected by six identical rows (solid lines) against analogous strips of ice (dashed lines), over a range of the scaled wavenumber $K = k_0/\pi$. The ice is of non-dimensional thickness $D = 0.02$, and the rows and strips are $l = 0.2$ apart. The non-dimensional radius is (a, d) $a = 0.15$, (b, e) $a = 0.3$ and (c, f) $a = 0.45$, with the incident wave angle set as $(a\text{–}c)$ $\vartheta = 0$ and $(d\text{–}f)$ $\vartheta = 60°$.

attainment of grazing incidence, at $K \approx 1.4$, by the geometry containing strips of ice, for which no propagating wave is induced in the ice and consequently all energy is reflected, a phenomenon that is not present in the multiple-row model. It appears from these results that in all but the $a = 0.15$ case for which the normally incident wave causes stronger reflection, the angle of incidence has little effect on the overall amount of energy reflected in the chosen range of wavenumbers. However, the chosen angle does vary the number and position of the maxima produced by the arrays.

To construct the scattering caused by multiple rows, in this work we have considered interactions of both the propagating waves and a finite number of the evanescent waves, so that we produce the full-linear solution to an arbitrary degree of accuracy. However, as evanescent waves decay rapidly away from the rows, it is expected that for sufficiently spaced rows, the only non-trivial interactions will involve the propagating waves. It is a simple matter to investigate this by restricting the scattering matrix $\boldsymbol{S}$ to contain only entries pertinent to the propagating waves and basing our interaction theory of the approximate transfer matrix that ensues. This method is often known as a WSA and is standard in scattering by multiple ice floes (see Bennetts *et al.* 2009*a*, for instance), as its use allows for a reduction in the numerical cost of calculating interactions and it is also possible for some analytical insight to be gained.

Figure 4 compares the value of the reflected energy produced by the WSA against that of the full approximation. Figure 4(*a*) plots E as a function of scaled wavenumber K, using an incident wave that travels at the angle $\vartheta = 60°$ with respect to the *x*-axis and for geometry consisting of identical rows of non-dimensional radius $a = 0.45$ and thickness $D = 0.02$ and equi-spaced such that $l = 0.2$. Results are shown for $M = 2, 4$ and 6 rows. The performance of the WSA here is excellent, with its results virtually overlapping those of the full approximation over the range of chosen wavenumbers. Slight deviations are seen only for the larger wavenumbers ($K > 2$), and there is no evidence of accumulation of errors as the number of rows is increased.
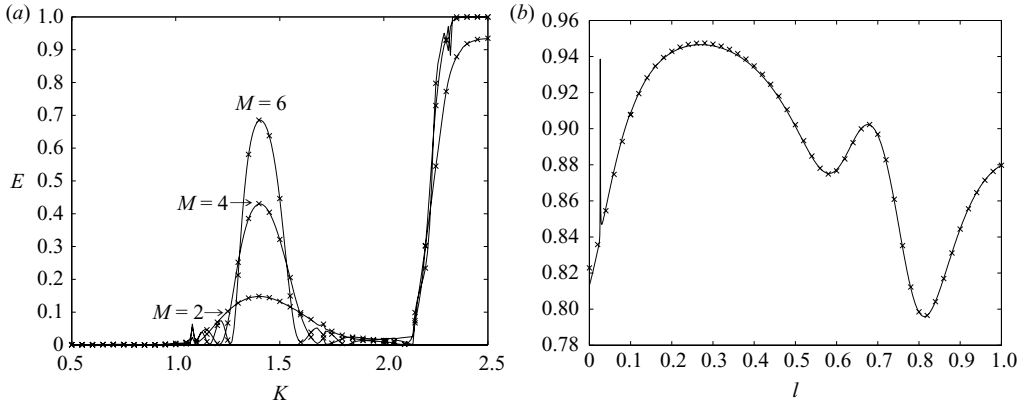
FIGURE 4. Comparison of the reflected energy, E, produced by the WSA (crosses) against that of the full approximation (solid curves). In (a) the geometry consists of $M = 2, 4$ and 6 identical rows of floes of non-dimensional radius $a = 0.45$ and thickness $D = 0.02$, that are equi-spaced with $l = 0.2$, and E is given as a function of scaled wavenumber $K = k_0/\pi$. In (b) $M = 2$ of these rows is used and E, as a function of their non-dimensional separation $0 < l < 1$, is plotted for $K = 2.5$. The incident angle is $\vartheta = 60°$ throughout.

In figure 4(b) the energy is plotted for the largest wavenumber in our chosen range ($K = 2.5$) using the two-row geometry considered in figure 4(a) but with the non-dimensional distance between the rows now varied over the interval $0 < l < 1$. Even for this relatively large wavenumber, the accuracy of WSA is generally exceptional. With the spacing as small as $l = 0.05$ the deviation between the WSA and the full approximation is minimal. As the rows move away from one another accuracy improves, so that by $l \approx 0.65$ the two are indistinguishable. Although, conversely, the accuracy of the WSA diminishes as the rows become very close, the error is still only marginal, except for within a small interval of distances centred around the point $l = 0.0264$. Here the full approximation displays a spike that is not reproduced by the WSA. This implies that for closely spaced rows and a sufficiently large wavenumber, it is possible for the interactions of the evanescent waves to produce a near resonance that affects the magnitude of the energy reflected by the rows, which in order to capture in our solution method requires the use of the full transfer matrices.

Note that in the previous figures that plot energy against the scaled wavenumber, K, relatively large responses over certain intervals are prominent. This is particularly evident in figure 4(a), in which we see the build-up of reflected energy as the number of rows is increased around the points $K \approx 1.4$ and $K \approx 2.5$. Within a periodic structure, the phenomenon of growth of reflected energy when the number of constituent periods increases is known as Bragg resonance. Bragg resonance is well established in a number of research areas and has recently been shown to occur strongly in scattering by two-dimensional periodic variations embedded in a continuous ice sheet (see Bennetts *et al.* 2009a).

In figure 5 we further investigate the occurrence of Bragg resonance in our multiple-row model by utilizing the WSA. Figure 5(a) shows the energy carried by the individual reflected waves, $|R_q|^2$ ($q \in Q$), using both the WSA and the full approximation. The geometry is periodic and consists of $M = 4$ rows of floes with radius $a = 0.45$, thickness $D = 0.02$ and the rows spaced so that $l = 0.2$. This is forced by an incident wave that propagates parallel to the x-axis ($\vartheta = 0$), which for $K > 2$ induces two extra
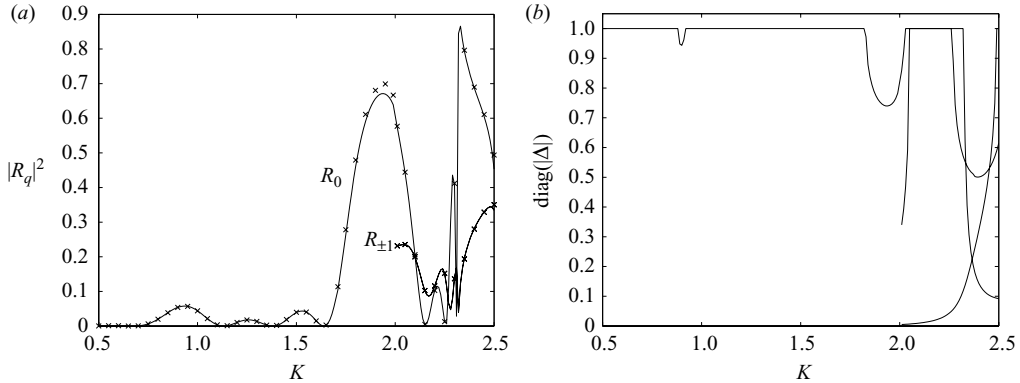
FIGURE 5. An investigation of the Bragg resonance produced by identical and equi-spaced rows of floes. In (*a*) the energy of the reflected waves, $|R_q|^2$ ($q \in Q$), produced by $M = 4$ rows using the WSA (crosses) and the full approximation (solid line) as a function of scaled wavenumber $K = k_0/\pi$, is plotted. The floes are of non-dimensional thickness $D = 0.02$ and radius $a = 0.45$, and the rows have the non-dimensional separation $l = 0.2$. The corresponding moduli of the diagonal entries of the matrix Δ used in the WSA are displayed in (*b*).

propagating waves with amplitudes $R_{\pm 1}$. Due to the symmetry of the problem these waves are merely reflections of one another in the *x*-axis, implying that $R_1 = R_{-1}$.

As we have seen previously, the accuracy of the WSA is excellent for all K in the chosen interval, although here it does slightly overestimate the peak centred around $K \approx 1.94$. Even for this small number of rows, appreciable Bragg resonance over large intervals of K are manifest in the peak just beneath $K = 1$, with the above-mentioned peak just beneath $K = 2$ and for $K > 2.35$. These resonances are associated to the so-called Bragg values $v_{0,0} = \pi/\hat{l}$, $v_{0,0} = 2\pi/\hat{l}$ and $v_{0,0} + v_{0,1} = 4\pi/\hat{l}$ respectively (see Porter & Porter 2001), where $\hat{l} = 2a + l = 1.1$ is the periodicity in the *x*-direction. In this problem, these Bragg values occur for the scaled wavenumbers $K = 0.9091$, $K = 1.8182$ and $K = 2.37$ respectively. The resonance caused by $v_{0,0} + v_{0,1} = 2\pi/\hat{l}$, which occurs just after the additional waves cut-in at $K = 2$, would appear to be overridden by that of $v_{0,0} = 2\pi/\hat{l}$. It is common in problems in which significant scattering occurs, such as this one, that resonances are centred close to Bragg values, rather than at Bragg values themselves. Here we see a tendency for the resonance to be centred at longer wave periods than the Bragg value would indicate.

We can examine the production of Bragg resonance by studying the eigenvalues of the transfer matrix used to produce the WSA. Drawing inferences from this restricted matrix is a far more appealing proposition than analysing its counterpart for the full approximation. Figure 5(*b*) displays the magnitude of the eigenvalues that make up the diagonal entries of the matrix Δ, that is the eigenvalues that lie within the unit circle or on the unit circle and above the real axis. As the size of the transfer matrix corresponds to the number of propagating waves, Δ is a scalar for $K < 2$, whereas Δ contains three eigenvalue entries for $K > 2$.

It is clear that the resonances seen in figure 5(*a*) correspond to intervals in which all of the eigenvalues lie within the unit circle. In such cases $\Delta^M \approx 0$ for large enough M, and therefore, with reference to the form of the scattering matrix given in (3.14), we can deduce that the transmitted amplitudes $T \approx 0$. When only a solitary wave is transmitted by the rows $T \equiv T_0$, and we can easily deduce through energy conservation that the magnitude of the corresponding reflected wave will be $|R_0| \approx 1$ for a sufficient
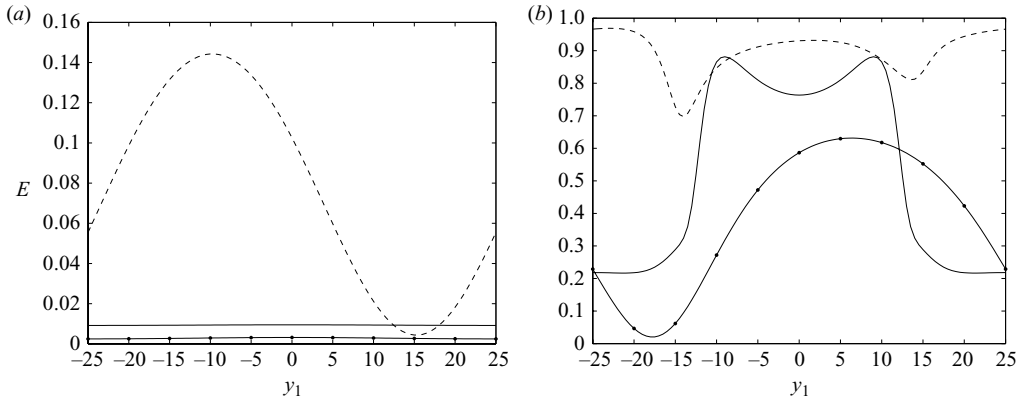
FIGURE 6. The reflected energy, E, for $M = 2$ identical rows of floes with a shift introduced in the y-direction. The non-dimensional thickness $D = 0.02$, radius $a = 0.45$ and row separation $l = 0.2$ are used. The reflected energy is plotted as a function of the shift y_1 for the three incident angles $\vartheta = 0$ (solid line), $\vartheta = 30°$ (dashed line) and $\vartheta = 60°$ (dotted line), with the scaled wavenumber fixed as $K = 1.25$ in (*a*) and $K = 2.5$ in (*b*).

value of M. Therefore, it can be inferred that the two Bragg resonances in figure 5(*a*) beneath $K = 2$ will grow still further if the number of rows used is increased, with clearly fewer additional rows needed for the second resonance than the first.

If more than one propagating wave is reflected, the energy is distributed amongst these waves, and although we will find that $E \approx 1$ when $\boldsymbol{T} \approx 0$, it does not follow that $|R_q| = 1$ ($q \in Q$). Instead, their values can be sought via expression (3.14), and in doing so, we find that in contrast to the two other resonances, the resonance above $K = 2$ has already converged to this bound. It thus appears that for multiple rows, Bragg resonance is greater for larger values of wavenumber. This is contrary to many previous studies in which the primary Bragg resonance is usually the strongest. What is seen here can be attributed to the increasing reflection that occurs at an ice edge as the wavenumber gets larger.

Thus far, the geometrical configurations for which we have presented results have been restricted to only those that involve identical rows. However, our model has been constructed so that more general geometries can be considered. In particular, rows may differ through the thickness and radius of their constituent floes. Furthermore, the spacing of the rows may be varied and their alignment altered by introducing shifts in the y-direction. It is of interest to observe how the addition of such inhomogeneities affects the scattering process, especially in respect to the production of resonances.

We begin by investigating the effects of a shift in the y-direction on the energy reflected by multiple rows. Figure 6 plots the energy reflected by two identical rows, as a function of the alignment parameter y_1, for the three incident wave angles $\vartheta = 0$, $30°$ and $60°$. The non-dimensional thickness of the floes used here is $D = 0.02$, with their non-dimensional radius $a = 0.45$ and the row spacing such that $l = 0.2$.

In figure 6(*a*) results are shown for the scaled wavenumber $K = 1.25$. It is striking that only the energy of the $\vartheta = 60°$ incident wave varies when the alignment of the rows changes. Such behaviour is to be expected though, as incident waves of angles $\vartheta = 0$ and $30°$ do not generate any additional angles between the rows for which waves may propagate, other than that of the incident wave. Thus, the interactions between rows are dominated by propagating waves travelling in a single plane, meaning that the nature of the problem is essentially two-dimensional and any shift in the
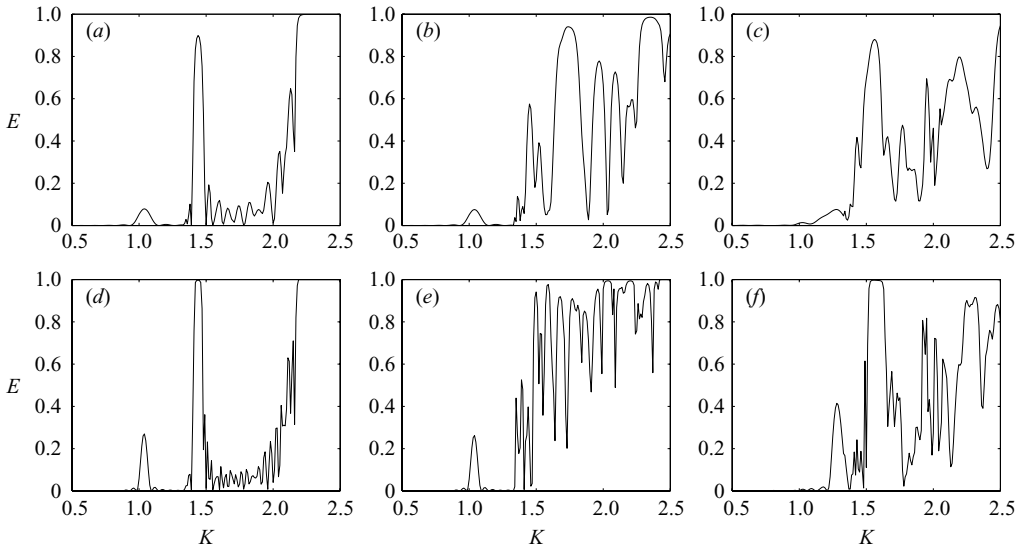
FIGURE 7. Comparison of the reflected energy, E, as a function of $K = k_0/\pi$ produced by (a, d) a homogeneous array with averaged values of (b, e) unaligned and (c, f) irregularly spaced rows. The rows are identical with non-dimensional thickness $D = 0.02$ and radius $a = 0.45$. When the rows are equi-spaced, their separation is $l = 0.2$, and when they are irregularly spaced the average separation remains consistent. The case of $M = 10$ rows is shown in $(a–c)$ and that of $M = 20$ rows in $(d–f)$. The incident wave angle is $\vartheta = 30°$.

y-direction will be trivial. This contrasts with the $\vartheta = 60°$ incident wave that produces two propagating wave angles between the rows, and consequently interactions will depend on their alignment.

The problems considered in figure 6(b) are similar to those of figure 6(a) but for a larger value of the scaled wavenumber, $K = 2.5$. For all three incident waves, multiple propagating wave angles are generated between the pair of rows, and it can be seen that changes in alignment can cause large variations in the energy that they reflect. One additional angle arises for the $\vartheta = 30°$ incident wave, and the shape of the corresponding curve appears sinusoidal, which is similar to the $\vartheta = 60°$ curve of figure 6(a) that shares the same number of propagating wave angles, whereas the normally incident wave and the incident wave of angle $\vartheta = 60°$ each produce two additional wave angles, and this results in complicated behaviour of the energy reflected by the rows as the alignment changes, with both displaying regions of high variation and of negligible change.

By incorporating inhomogeneities, such as non-alignments, in the properties of the array, it is expected that resonant effects will be moderated, and we will thus find a better representation of how waves are scattered in the MIZ. Following our investigation of introducing a shift in the y-direction between two rows, in figure 7 we look at the effects of changing the position of rows, in respect to their alignment and separation, in a larger array. Over a range of the scaled wavenumber K, figure 7($a–c$) and figure 7($d–f$) both compare the energy of a $\vartheta = 30°$ incident wave reflected by a homogeneous array composed of identical, equi-spaced and aligned rows with two similar arrays, one containing variations in its alignment, the other in its row separation. The results given for these inhomogeneous arrays use the average of 100 random simulations. All of the arrays use the non-dimensional ice thickness $D = 0.02$
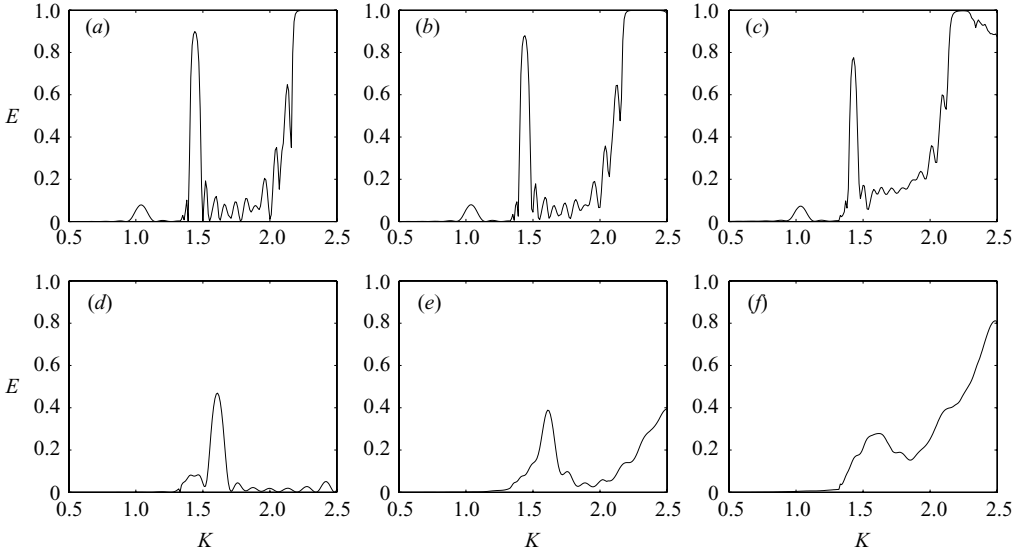
FIGURE 8. Comparison of the reflected energy, E, as a function of $K = k_0/\pi$ produced by a homogeneous array with averaged values of similar arrays but containing non-identical rows. Panels $(a\text{--}c)$ show $M = 10$ rows of non-dimensional radius $a = 0.45$, equi-spaced with $l = 0.2$, (a) for identical rows $D_1 = \ldots = D_{10} = 0.02$, and averages at which the thickness ranges (b) from $D = 0.011$ to $D = 0.029$ and (c) from $D = 0.002$ to $D = 0.038$. Panels $(d\text{--}f)$ show $M = 10$ rows of non-dimensional thickness $D = 0.02$, equi-spaced with $l = 0.2$, (d) for identical rows of radius $a_1 = \ldots = a_9 = 0.3$, and averages at which the radius ranges (e) from $a = 0.225$ to $a = 0.375$ and (f) from $a = 0.15$ to $a = 0.45$. The incident wave angle is $\vartheta = 30°$.

and radius $a = 0.45$. The equally spaced arrays use the separation $l = 0.2$, and the unequally spaced arrays are restricted so that their average spacing is also 0.2.

In figure 7$(a\text{--}c)$ $M = 10$ rows are used, and in figure 7$(d\text{--}f)$ the array is made up of $M = 20$ rows. As predicted by figure 6(a), for values of wavenumber small enough that only one propagating wave angle is generated, here approximately $K < 1.3$, the reflection caused by the arrays containing shifts in the y-direction is identical to that of the homogeneous array. In comparison, the arrays with non-uniform row separations display different properties than that of the homogeneous array, with, most notably, the primary resonance, around $K = 1.05$, absent. For larger wavenumbers both the unaligned and the unequally spaced arrays predict entirely different reflection characteristics than those of the homogeneous array. Whereas the latter is dominated by the two resonances, for the inhomogeneous array the energy distribution is more evenly spread over the range of wavenumbers in a series of peaks. Presumably the noise present in these averaged results is a product of the length scales that remain in the arrays and could be eradicated by sampling from a more diverse set. An estimate of the reflection caused by the MIZ as a function of wavenumber could then be extracted, and this idea will provide the basis for a forthcoming work.

Further inhomogeneities are studied in figure 8, which here take the form of differences in the properties of the floes. In figure 8$(a\text{--}c)$ we consider the effects on the reflected energy of a changing floe thickness in the different rows. One curve shows the reflection of a $\vartheta = 30°$ incident wave, produced by a homogeneous array comprising $M = 10$ identical rows, with non-dimensional ice thickness $D = 0.02$ and radius $a = 0.45$, equi-spaced by the non-dimensional length $l = 0.2$. For the

two additional curves the problem is identical, except that the thickness of the floes in each row is different. The non-dimensional thicknesses are chosen from either the set $D_m \in \{0.011, 0.013 \dots, 0.029\}$ or the set $D_m \in \{0.002, 0.006, \dots, 0.038\}$ ($m = 1, \dots, 10$), so that their mean thickness, $D = 0.02$, matches the thickness of the floes in the homogeneous array.

The curves displaying the reflection by the geometry with varying thickness take the average of 100 random samples of the order of the rows. It is apparent that the redistribution of the ice thickness amongst the rows does not alter the amount of energy reflected by the array to a great extent, with the reflection from the array in which thicknesses are chosen from the least perturbed set being virtually indistinguishable from that of the identical rows. In particular, the position of the two Bragg resonances, which appear beneath $K = 1.5$ and $K = 2.5$ respectively, remain for the arrays with varying thickness. This is perhaps unsurprising, as the same length scale $\hat{l}$ exists in all three problems. We do however note that the resonances are damped in the case of the larger variations.

Figure 8(*d–f*) compares $M = 9$ identical rows of floes with non-dimensional thickness $D = 0.02$ and radius $a = 0.3$, against similar geometries but ones for which the radius is varied. Here, the radii are selected from either the set $a_m \in \{0.225, 0.3, 0.375\}$ or the set $a_m \in \{0.15, 0.3, 0.45\}$ ($m = 1, \dots, 9$), restricted so that their average is fixed at $a = 0.3$, as in the identical-row geometry, and again the curves presented use an average of 100 randomly generated instances. As in figure 8(*a–c*), in all geometries the rows are equi-spaced with $l = 0.2$ and the incident wave propagates at the angle $\vartheta = 30°$ with respect to the x-axis.

We again see that the resonance that exists for the homogeneous array persists in the arrays containing rows of different properties. However, the changes to the radius here produce more significant effects than changes to the thickness seen in figure 8(*a–c*), and the resonance becomes increasingly damped in amplitude and spreads over a larger interval of wavenumbers as the rows become more varied, which is due to changes in the length scale $\hat{l}$. A trend for increasing reflection also develops at the right-hand end of the range of wavenumbers and is far more prominent when the variation in the radii is larger. By including an increasing amount of variation in the radius of the floes, the quantity of energy reflected by the array appears to be tending towards a relatively steady growth as the wavenumber gets larger.

Changes to the properties of the floes can and will be considered along with the non-uniform spacings explored in figure 7 when designing models of MIZs. As we have just demonstrated, the introduction of variations in the radius of the floes used diminishes the effects of resonance that is produced in a homogeneous array. However, it appears that changes in the thickness of the floes around an average value are only of minimal importance.

5. Conclusions

In this work we have constructed a model of the scattering of ocean waves in the MIZ in the form of multiple rows of ice floes. Each row contains an infinite number of identical and equally spaced floes, and although the properties of the floes are permitted to vary between the rows, a common periodicity length scale was required. For the purposes of this study, the floes themselves were supposed to be circular and of uniform thickness, and an accurate Archimedean draught was incorporated.

To begin the solution procedure, the vertical coordinate was removed by applying an expansion in a finite set of modes within a variational principle. This left a finite

set of equations to be solved in the horizontal plane only, separated into the respective ice-covered and ice-free fluid domains. The solution to the multiple-row problem was then built up from that of the individual problems posed by its constituent rows, by recognizing that the waves incident on each row are those scattered by its adjacent rows.

For a single row, periodicity was applied, and this allowed the problem to be recast in a channel containing only a solitary floe. An analytical expression was then deduced for the unknowns within the disk of ice-covered fluid along with an integral expression for the unknowns in the free-surface portion of the channel. This integral expression was a simplification of that given in a previous work, which applied new identities for the matrix of Green's functions used to derive it, and led to vastly reduced numerics. The expressions in the two respective domains were then matched at their common boundary in order to complete the solution process.

By generalizing the forcing for each individual row to allow for evanescent waves, as well as all possible propagating waves, we constructed transfer matrices that give the amplitudes of the waves on one side of the row in terms of the amplitudes of the waves on the other side. These transfer matrices provided a simple iterative means of combining the rows to form the solution for the full array. Further simplifications were seen to be possible if the rows were identical and equally spaced.

Our numerical results were concentrated on the energy reflected by multiple rows over a range of wavenumbers. A preliminary investigation was made into the differences between the multiple-row model and an analogous two-dimensional model, in which waves are scattered by strips of ice. It was found that for a normally incident wave the scattering properties of the two geometries were similar, although the strips generally reflect more energy and this tendency was exacerbated for smaller floes with a larger floe spacing within the rows, whereas for an obliquely incident wave, unlike the strips, the rows possess no limit in which propagating waves cannot be transmitted, and consequently their reflection properties differ greatly.

We also compared our interaction theory, which synthesizes the interactions of both the propagating waves and a finite number of the evanescent waves, producing the full-linear solution to any given tolerance, with a WSA that considers only the interaction of the propagating waves. The WSA was shown to be highly accurate, even for closely spaced rows. However, it could not reproduce certain features attributed to the interactions of evanescent waves for large wavenumbers and proximate rows.

Using the WSA, we investigated the production of Bragg resonance by homogeneous arrays of identical and equally spaced rows. These resonances, that are prominent for relatively few rows and occur over large intervals of wavenumbers, were seen to be related to the departure of all of the eigenvalues of the transfer matrix used in the WSA from the unit circle. It was also found that the resonances tended to occur for longer waves than theory predicts, and unlike the findings of other investigations of which we are aware, here the strength of the resonance became greater with increasing wavenumber.

In the final set of results we were concerned with comparing the reflection produced by homogeneous and inhomogeneous arrays. Changes in the row alignment, row spacing, floe thickness and floe radius were all considered independently, using averages of randomly sampled sets. With the exception of variations to the floe thickness, the introduction of all of these non-uniformities caused significant alterations in the behaviour of the reflected energy as a function of wavenumber and, in particular, minimized the effects of Bragg resonance.

The solution method outlined herein is now available for constructing simulations of a real MIZ. As we have seen, the current model would predict very different

attenuation rates from that of the two-dimensional models used to date, especially for large wavenumbers and obliquely incident waves. The MIZ exists over hundreds of kilometres, containing a vast number of individual floes, and a realistic model would involve a large number of rows with differing properties. It has been demonstrated here that averaging over a number of similar geometrical configurations, particularly in respect to the spacing and size of the floes and alignment of the rows, helps to eliminate the occurrences of Bragg resonance that can otherwise pollute data when recreating a natural phenomenon such as the MIZ. It would also be pertinent to use a WSA, which was shown in this work to provide excellent accuracy, in order to reduce the numerical cost. Work on this project is already underway.

REFERENCES

BENNETTS, L. G., BIGGS, N. R. T. & PORTER, D. 2007 A multi-mode approximation to wave scattering by ice sheets of varying thickness. *J. Fluid Mech.* **579**, 413–443.

BENNETTS, L. G., BIGGS, N. R. T. & PORTER, D. 2009*a* The interaction of flexural-gravity waves with periodic geometries. *Wave Mot.* **46**, 57–73.

BENNETTS, L. G., BIGGS, N. R. T. & PORTER, D. 2009*b* Wave scattering by an axisymmetric ice floe of varying thickness. *IMA J. Appl. Math.* **74**, 273–295.

BENNETTS, L. G. & SQUIRE, V. A. 2009 Linear wave forcing of an array of axisymmetric ice floes. *IMA J. Appl. Math.* In press.

CAVALIERI, D. J., PARKINSON, C. L. & VINNIKOV, K. Y. 2003 30-year satellite record reveals contrasting Arctic and Antarctic decadal sea ice variability. *Geophy. Res. Lett.* **30** (18). DOI: 10.1029/2003GL018031.

CHAMBERLAIN, P. G. & PORTER, D. 1995 Decomposition methods for wave scattering by topography with application to ripple beds. *Wave Mot.* **22**, 201–214.

CHOU, T. 1998 Band structure of surface flexural-gravity waves along periodic interfaces. *J. Fluid Mech.* **369**, 333–350.

DIXON, T. W. & SQUIRE, V. A. 2001 Energy transport in the marginal ice zone. *J. Geophys. Res.* **106**, 19917–19927.

KOHOUT, A. L. & MEYLAN, M. H. 2008 An elastic plate model for wave attenuation and ice floe breaking in the marginal ice zone. *J. Geophys. Res.* **113**, C09016. DOI: 10.1029/2007JC004434.

KOHOUT, A. L., MEYLAN, M. H., SAKAI, S., HANAI, K., LEMAN, P. & BROSSARD, D. 2007 Linear water wave propagation through multiple floating elastic plates of variable properties. *J. Fluids. Struct.* **23** (4), 649–663.

LINTON, C. 1998 The Green's function for the two-dimensional Helmholtz equation in periodic domains. *J. Engng Math.* **33**, 377–402.

LINTON, C. M. & THOMPSON, I. 2007 Resonant effects in scattering by periodic arrays. *Wave Mot.* **44** (3), 165–175.

MCPHEDRAN, R. C., BOTTEN, L. C., ASATRYAN, A. A., NICOROVICI, N., ROBINSON, P. & STERKE, C. M. D. 1999 Calculation of electromagnetic properties of regular and random arrays of metallic and dielectric cylinders. *Phys. Rev.* E **60** (6), 7614–7617.

MEYLAN, M. H. & MASSON, D. 2006 A linear Boltzmann equation to model wave scattering in the marginal ice zone. *Ocean Model.* **11**, 417–427.

PETER, M. A. & MEYLAN, M. H. 2004 Infinite depth interaction theory for arbitrary floating bodies applied to wave forcing of ice floes. *J. Fluid Mech.* **500**, 145–167.

PETER, M. A. & MEYLAN, M. H. 2007 Water-wave scattering by a semi-infinite periodic array of arbitrary bodies. *J. Fluid Mech.* **575**, 473–494.

PORTER, R. & PORTER, D. 2001 Interaction of water waves with three-dimensional periodic topography. *J. Fluid Mech.* **434**, 301–335.

ROTHROCK, D. A., YU, Y. & MAYKUT, G. A. 1999 Thinning of the Arctic sea-ice cover. *Geophys. Res. Lett.* **26** (23), 3469–3472.

SERREZE, M. C., HOLLAND, M. M. & STROEVE, J. 2007 Perspectives on the Arctic's shrinking sea-ice cover. *Science* **315** (5818), 1533–1536. DOI: 10.1126/science.1139426.

SQUIRE, V. A. 2007 Of ocean waves and sea-ice revisited. *Cold Reg. Sci. Technol.* **49**, 110–133.

SQUIRE, V. A., DUGAN, J. P., WADHAMS, P., ROTTIER, P. J. & LIU, A. K. 1995 Of ocean waves and sea ice. *Annu. Rev. Fluid Mech.* **27**, 115–168.

WADHAMS, P., SQUIRE, V. A., EWING, J. A. & PASCAL, R. W. 1986 The effect of the marginal ice zone on the directional wave spectrum of the ocean. *J. Phys. Oceanogr.* **16** (2), 358–376.

WADHAMS, P., SQUIRE, V. A., GOODMAN, D. J., COWAN, A. M. & MOORE, S. C. 1987 The attenuation of ocean waves in the marginal ice zone. *J. Geophys. Res.* **93** (C6), 6799–6818.